Research Article ISSN 2766-2624

Advances in Earth and Environmental Science

Cooling The Sahel's Expanding Cities: Land Surface Temperature Dynamics and Urban Resilience Planning in Nigeria's Upper Benue River Basin

Joshua Ma'aku Mark[1], Yakubu Stephen Zirankuthii[2], Oruonye, E. D[2*] and Musa Hassan[3]

[1]*Taraba State Geographic Information Services (TAGIS), Taraba State, Nigeria.*

[2]*Department of Geography, Taraba State University, Jalingo, Nigeria.*

[3]*Department of Surveying and Geo-informatics, Hassan Usman Katsina Polytechnic, Katsina.*

***Corresponding author**

Emeka Daniel Oruonye,
Department of Geography, Taraba State University, Jalingo, Nigeria.

Submitted: 17 Jun 2026; **Accepted:** 23 Jun 2026; **Published:** 10 Jul 2026

Citation: Mark, J. M., Zirankuthii, Y. S., Oruonye, E.D., & Musa Hassan (2026). Cooling the Sahel's expanding cities: Land surface temperature dynamics and urban resilience planning in Nigeria's Upper Benue River Basin. *.Adv Earth & Env Sci; 7*(3):1-16.
DOI : https://doi.org/10.47485/2766-2624.1094

Abstract
The Sahel region of Africa is experiencing rapid urbanization concurrent with intensifying climate change, yet the spatial dynamics of extreme heat in semi-arid urban environments remain critically understudied. This research characterizes land surface temperature (LST) dynamics and thermal hotspots across the Upper Benue River Basin (UBRB) in northeastern Nigeria from 2015 to 2025 using Landsat and MODIS thermal imagery integrated with land use/land cover classification and spatial statistical analysis (Getis-Ord Gi). Results reveal that basin-wide mean dry season LST increased from 36.8°C in 2015 to 38.5°C in 2025, representing a statistically significant warming of 1.7°C over the decade (Sen's slope = 0.17°C/year, $p < 0.01$), with urban centers warming at rates 2–3 times faster than surrounding rural areas. Thermal hotspots (LST ≥ 90th percentile, >41.2°C) now cover 2,530 km² (6.4% of the basin), concentrated in Taraba State (1,240 km², mean 44.6°C) around the Jalingo urban cluster and degraded riparian zones, Adamawa State (980 km², mean 43.9°C) in the Yola North–Jimeta conurbation and Numan industrial corridor, and Gombe State (310 km², mean 42.3°C) in the Gombe urban core. Built-up areas across Jalingo, Yola North, Jimeta, Numan, and Gombe exhibit mean LST of 42.6°C compared to 35.2°C for vegetated surfaces, with NDVI and impervious surface fraction explaining 79% of LST variance. Critically, 847 km² (33.5%) of thermal hotspot area overlaps with high flood susceptibility zones, placing an estimated 1.2 million residents—two-thirds in informal settlements—in compound hazard conditions, with the Jalingo floodplain showing 74% of built-up area affected, the Yola North–Jimeta corridor showing 65%, and Gombe low-lying sections showing 52%. The 38% expansion of built-up area and 15% decline in vegetation over the decade confirm unplanned urbanization as the primary driver of intensifying heat risk, while the Getis-Ord Gi* analysis confirms statistically significant ($p < 0.01$) high-LST clusters with Global Moran's I of 0.87 ($p < 0.001$), indicating extremely strong spatial autocorrelation where hotspots coalesce into large contiguous clusters that amplify the Urban Heat Island effect through positive feedback mechanisms. These findings provide the empirical foundation for targeted nature-based interventions including urban greening in Jalingo, Yola, Numan, Jimeta, and Gombe, heat-resilient building codes requiring reflective roofing and permeable surfaces, compound hazard-informed land use planning that prohibits new residential construction in very high hazard zones, and an urban climate monitoring system to enhance resilience in the UBRB and analogous Sahelian cities.*

Keywords: Compound Hazard, Land Surface Temperature, Upper Benue River Basin, Urban Heat Island, Sahel Urbanization, Thermal Hotspots.

Introduction
The Sahel region of Africa represents one of the world's most vulnerable frontiers in the context of climate change and rapid urbanization. Stretching across the continent from Senegal in the west to Sudan in the east, the Sahelian belt is characterized by semi-arid conditions, pronounced seasonal variability, and a population that is simultaneously among the fastest-growing and most economically disadvantaged on Earth (IPCC, 2022; United Nations, 2022). Within this region, Nigeria stands as a critical case: as Africa's most populous nation and largest economy, it is experiencing urban growth rates exceeding 4% annually, with projections indicating that nearly 70% of Nigerians will reside in urban centers by 2050 (World Bank, 2023; National Population Commission, 2023). This demographic transition, while indicative of economic transformation, unfolds against a backdrop of accelerating climate change that poses unprecedented challenges to urban sustainability and human well-being. Among the most pressing climate-related threats facing Sahelian cities is the intensification of extreme heat. The Intergovernmental Panel on Climate Change (IPCC) Sixth Assessment Report documents with high confidence that heatwaves have become more

frequent and intense across West Africa since 1960, a trend projected to accelerate under all emission scenarios (IPCC, 2021; Dosio et al., 2019). Urban environments amplify this hazard through the Urban Heat Island (UHI) effect, whereby the replacement of vegetated, permeable surfaces with built, impervious materials elevates surface and air temperatures by 3–7°C relative to surrounding rural areas (Oke et al., 2017; Zhao et al., 2018). The convergence of background climatic warming with localized UHI intensification creates what epidemiologists term "compounded heat risk", a condition where physiological heat stress exceeds adaptive capacity, with documented consequences including elevated morbidity and mortality, reduced labor productivity, increased energy demand, and degraded air quality (Patz et al., 2020; Romanello et al., 2022; He et al., 2021).

The Upper Benue River Basin (UBRB) in northeastern Nigeria embodies these intersecting challenges in acute form. The basin, spanning approximately 154,329 km² across Taraba, Adamawa, Gombe, and Bauchi States, supports a rapidly growing population, with urbanization rates among the highest in northern Nigeria (Odiji et al., 2021). The region's climate is characterized by a pronounced dry season (November–March) during which temperatures routinely exceed 38°C, and the ITCZ-driven wet season (April–October) that brings intense rainfall events increasingly associated with flash flooding (Odiji et al., 2021). This seasonal duality, extreme heat during the dry season and floods during the wet season places urban populations in a continuous state of climate risk, with limited seasonal respite. Despite growing recognition of urban heat as a critical climate hazard, significant knowledge gaps persist regarding the spatial dynamics, drivers, and human implications of extreme heat in Sahelian cities. The majority of UHI research has concentrated on temperate and tropical megacities in Asia, Europe, and North America, with comparatively limited empirical investigation of the distinct biophysical and socio-economic contexts characteristic of Sahelian urban systems (Bartesaghi-Koc et al., 2018). This geographical bias is consequential because the drivers of UHI intensity differ fundamentally in semi-arid environments: where vegetated cooling dominates in humid climates, albedo effects and soil moisture availability become paramount in drylands (Manoli et al., 2019). Without localized empirical evidence, urban planners in the UBRB lack the scientific foundation necessary to prioritize heat mitigation interventions, allocate scarce resources effectively, or advocate for climate-adaptive land use policies.

Existing studies within Nigeria have focused predominantly on coastal and southern cities including Lagos, Port Harcourt, Ibadan, and Benin City, which experience different climatological regimes characterized by higher humidity, denser vegetation cover, and less extreme diurnal temperature ranges (Balogun et al., 2020; Nwokoro & Ogunbiyi, 2019). The semi-arid cities of northeastern Nigeria, including Jalingo, Yola, Numan, and Jimeta, remain severely understudied despite their documented vulnerability and rapid expansion (Audu & Jibril, 2022; Abubakar & Yamusa, 2021). This geographical disparity leaves planners and policymakers in the region without localized, evidence-based information necessary to guide interventions. Furthermore, previous research has tended to analyze extreme heat and flooding as separate hazards, despite their frequent co-occurrence and synergistic effects on vulnerable populations (Raymond et al., 2020; Zscheischler et al., 2020). In the UBRB, the same low-lying, densely settled areas that experience the most severe flooding during the wet season also exhibit the highest land surface temperatures during the dry season, a compound vulnerability pattern that has received minimal empirical attention (Matthews et al., 2021; Bibi et al., 2022). There is little or no published study that has spatially overlaid thermal hotspot maps with flood susceptibility assessments for the UBRB, limiting understanding of compound hazard exposure and the potential for integrated resilience strategies that address both hazards simultaneously rather than through siloed, potentially contradictory interventions. Additionally, there exists a critical gap in operationalizing remote sensing-derived thermal information for urban planning and resilience policy. While satellite-based land surface temperature (LST) products are widely available, their translation into actionable planning tools, such as vulnerability maps, intervention prioritization frameworks, and land use zoning guidelines, remains limited in West African contexts (Sobrino et al., 2020; Adepoju & Adelabu, 2020). There is little or no study that has systematically characterized decadal LST trends across the UBRB from 2015 to 2025, leaving uncertainty regarding whether and to what extent urban warming is accelerating relative to background climatic trends. Previous research has examined individual urban centers in isolation, preventing comparative assessment of how different urban forms, development histories, and landscape contexts mediate UHI intensity. The spatial distribution, intensity gradients, and land cover correlates of extreme thermal anomalies have not been quantitatively mapped at urban-relevant scales, nor has the connection between LST analysis and specific, actionable resilience interventions such as green corridor placement, cool roofing priorities, and floodplain reforestation been articulated for the UBRB context.

To address these interconnected gaps, this study aims to characterize land surface temperature dynamics and thermal hotspots across the Upper Benue River Basin to inform evidence-based urban resilience planning. Specifically, the study seeks to:

- quantify the spatial distribution and temporal evolution of land surface temperature across the UBRB from 2015 to 2025 using multi-temporal Landsat and MODIS thermal imagery, thereby establishing whether urban warming is accelerating and identifying the most thermally stressed areas;
- identify and classify thermal hotspots based on statistical thresholds (90^{th} percentile) and spatial clustering using the Getis-Ord Gi* statistic, quantifying their areal extent, intensity, and distribution by state and land cover class to enable targeted intervention prioritization;

- establish statistical relationships between LST and biophysical parameters including vegetation cover (NDVI), impervious surface fraction, distance to water bodies, and elevation to identify the primary drivers of thermal variability and inform nature-based solution design;
- assess the spatial overlap between thermal hotspots and flood-prone zones, quantifying the population and urban area exposed to compound heat-flood hazards and identifying priority zones for integrated resilience interventions; and
- derive planning-relevant recommendations for nature-based solutions including urban greening, riparian reforestation, and cool infrastructure targeted to the specific thermal and hydrological characteristics of the UBRB, thereby bridging the gap between remote sensing analysis and actionable urban policy.

This study contributes to the international literature on urban climate resilience in three principal ways. First, it extends the geographical coverage of UHI research into the understudied Sahelian context, providing empirical data from a region that is both highly vulnerable and rapidly urbanizing (Da, 2021; Silva, 2026). Second, it advances methodological approaches for integrating thermal remote sensing with flood hazard mapping, demonstrating a replicable framework for compound hazard assessment applicable across data-scarce regions of sub-Saharan Africa (Boeck et al., 2022; Burke et al., 2016). Third, it produces actionable planning products, including state-level hotspot statistics, land cover-specific thermal profiles, and prioritized intervention zones, that can directly inform urban development policies, disaster risk reduction strategies, and climate adaptation investments in the UBRB and analogous Sahelian urban systems. The remainder of this paper is organized as follows: Section 2 describes the study area, data sources, and analytical methodology including LST retrieval, land cover classification, hotspot analysis, and statistical procedures. Section 3 presents results on spatial LST patterns, temporal trends, thermal hotspot distribution, and LST-land cover relationships. Section 4 discusses these findings in the context of previous research, articulates implications for resilience planning, acknowledges study limitations, and proposes directions for future research. Section 5 concludes with summary findings and policy recommendations.

Methodology

Study Area Description

The Upper Benue River Basin (UBRB) is located in northeastern Nigeria, extending approximately between latitudes 6°02′N–11°36′N and longitudes 8°54′E–13°29′E (Fig. 1). The basin encompasses a total land area of approximately 154,329 km²(Odiji et al., 2021). The study area includes the entire upstream catchment of the Benue River and its major tributaries, including the Faro, Lamurde, Taraba, Suntai, Gongola, and Donga Rivers (Adeyeri et al., 2020).

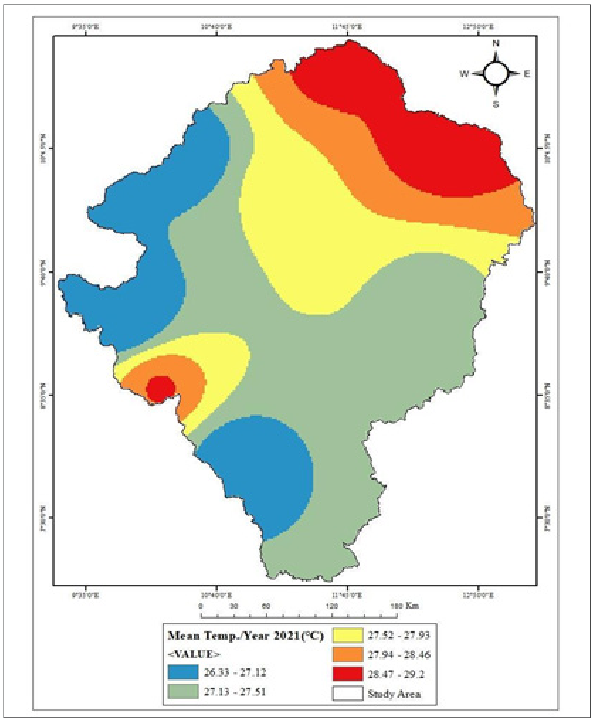

Figure 1. Temperature Distribution in 2021
Source: Joshua et al., 2023

The UBRB is characterized by a tropical savanna climate influenced by the seasonal migration of the Intertropical Convergence Zone (ITCZ). The region experiences distinct wet (April–October) and dry (November–March) seasons, with mean annual rainfall ranging from 700 mm to 1200 mm (Odiji et al., 2021). Mean annual temperatures vary between 24°C and 27°C (Odiji et al., 2021). Topographically, the basin is diverse: the eastern and southern margins are dominated by the Adamawa Plateau and Mambila Plateau (elevations of 1,000–1,500 m above sea level), while the central and western portions feature extensive floodplains and river valleys with elevations below 500 m (Joshua et al., 2023). This topographic heterogeneity significantly influences both hydrological processes (flood generation, drainage patterns) and thermal regimes (altitudinal temperature gradients, cold air drainage) (Zhou et al., 2019).

The basin supports a growing population with increasing urbanization in major centers. Key urban areas within the study domain include Jalingo (Taraba State), Yola North, Yola South (Adamawa State), Numan, Jimeta, and Gombe. These cities exhibit characteristic features of Sahelian urbanization: rapid informal settlement expansion, declining vegetation cover, inadequate drainage infrastructure, and high socio-economic vulnerability to climate extremes (World Bank, 2023).

Research Design and Analytical Framework

This study employed a quantitative, retrospective longitudinal design integrating remote sensing time-series analysis, geospatial modelling, and statistical inference to characterise land surface temperature dynamics and thermal hotspot distribution across the UBRB (Sobrino et al., 2020; Adepoju & Adelabu, 2020). The analytical framework comprised four sequential phases as adapted from standard protocols for urban heat island assessment in data-scarce regions (Lazzarini et al., 2021; Peng et al., 2020). Phase 1 involved data acquisition and preprocessing, including acquisition of satellite imagery (Landsat, MODIS), digital elevation models (SRTM DEM), and auxiliary datasets (land cover, population), followed by radiometric calibration, atmospheric correction, and geometric registration to ensure data consistency across the temporal domain (2015–2025). Phase 2 comprised land surface temperature retrieval, where LST was derived from thermal infrared bands using the single-channel algorithm for Landsat and split-window algorithm for MODIS, with LST time-series generated for dry season periods (February–March) to minimise confounding effects of cloud cover and seasonal variability (Jiménez-Muñoz & Sobrino, 2003; Wan & Dozier, 1996). Phase 3 involved thermal hotspot analysis, including identification and classification of thermal hotspots using a threshold-based approach (90th percentile LST) and spatial clustering using the Getis-Ord Gi* statistic, with hotspot extent, intensity, and spatial distribution quantified at state and settlement scales (Ord & Getis, 1995). Phase 4 consisted of land cover integration and statistical analysis, including overlay of LST layers with classified land use/land cover (LULC) maps to quantify thermal signatures of different cover types, with correlation and regression analyses conducted to establish relationships between LST and biophysical parameters including vegetation indices, impervious surface fraction, elevation, and proximity to water bodies (Zhou et al., 2019; Zhao et al., 2018). All geospatial analyses were conducted using ArcGIS Pro 3.2, QGIS 3.34, and the Google Earth Engine (GEE) platform, while statistical analyses were performed using R version 4.3.2 and Python 3.11 with libraries including NumPy, Pandas, Scikit-learn, and GeoPandas (Gorelick et al., 2017; R Core Team, 2023).

Data Sources and Acquisition

Satellite Data

Landsat archive (2015–2025) Level-2 Collection 2 Tier 1 surface reflectance and surface temperature products from Landsat 8 (Operational Land Imager/Thermal Infrared Sensor, OLI/TIRS) and Landsat 9 (OLI-2/TIRS-2) were acquired from the United States Geological Survey (USGS) EarthExplorer portal (https://earthexplorer.usgs.gov) (USGS, 2021). Key specifications include spatial resolution of 30 m (thermal bands resampled from 100 m to 30 m), temporal resolution of 16-day revisit cycle, spectral bands utilized including Band 10 (thermal infrared 1, 10.6 - 11.2 μm) for LST retrieval and Bands 2–7 (visible and near-infrared) for land cover classification and index calculation (Roy et al., 2014). Scene coverage included Paths 185 - 190 and Rows 51 - 55, ensuring complete basin coverage, with a total of 47 dry season scenes (February–March) acquired spanning 2015–2025.

MODIS Terra/Aqua (2015–2025) Moderate Resolution Imaging Spectroradiometer products MOD11A2 (Terra, 8-day composite LST) and MYD11A2 (Aqua, 8-day composite LST) Version 6.1 were obtained from the NASA LP DAAC (https://lpdaac.usgs.gov) (Wan et al., 2015). Specifications include spatial resolution of 1 km (resampled to 30 m for validation), temporal resolution of 8-day composites (4–6 scenes per month), and product quality assurance provided with QC layers for cloud cover, aerosol loading, and pixel reliability assessment over the period January 2015 to December 2025.

Sentinel-2 (2017–2025) multispectral imagery from Sentinel-2A and Sentinel-2B (European Space Agency) was used for high-resolution land cover classification and validation, with data accessed via Copernicus Open Access Hub (https://scihub.copernicus.eu) and GEE (Drusch et al., 2012). Specifications include spatial resolution of 10 m (visible and near-infrared) and 20 m (red edge, shortwave infrared), revisit frequency of 5 days (combined A and B), and cloud cover threshold of less than 20% per scene.

Ancillary Datasets

Digital Elevation Model (DEM) SRTM (Shuttle Radar Topography Mission) DEM Version 3 with 30 m spatial resolution was obtained from USGS EarthExplorer (Farr et al., 2007). This dataset was used for topographic normalization of LST (elevation - temperature relationships) and derivation of terrain attributes including slope, aspect, and topographic wetness index (Wilson & Gallant, 2000). Land cover reference data from the European Space Agency (ESA) WorldCover 2020 and 2025 products (10 m resolution, 11 land cover classes) were used as baseline classification layers (Zanaga et al., 2021). For the historical period (2015), Landsat-derived LULC maps were generated using supervised classification with ground truth validation points (Foody, 2002). Climate data including gridded climate variables (air temperature, precipitation, humidity) from ERA5-Land reanalysis (European Centre for Medium-Range Weather Forecasts, ECMWF) were used for atmospheric correction and contextual interpretation of LST patterns, with spatial resolution of 0.1° (approximately 9 km) and hourly temporal resolution (Hersbach et al., 2020). Administrative boundaries, including State and Local Government Area (LGA) boundary shapefiles, were obtained from the National Population Commission of Nigeria and the Global Administrative Areas (GADM) database (https://gadm.org) (GADM, 2022).

Data Preprocessing

All acquired Landsat scenes underwent standardized preprocessing using the USGS Level-2 processing stream, which includes radiometric calibration converting digital numbers (DN) to top-of-atmosphere (TOA) reflectance and radiance, atmospheric correction applying the Land Surface Reflectance Code (LaSRC) for Landsat 8 and Landsat 9, which corrects for atmospheric scattering and absorption using MODIS-derived water vapor and aerosol information (Vermote et al., 2016), cloud masking applying the CFMask (Cirrus Function of Mask) algorithm to identify and mask clouds, cloud shadows, and snow/ice pixels, with only scenes having less than 20% cloud cover within the study area retained (Wei et al., 2020), and geometric registration, with all scenes co-registered to the UTM Zone 32N projection (WGS84 datum) with RMSE less than 0.5 pixels (15 m) (USGS, 2021). For MODIS data, the MOD11A2 and MYD11A2 products were already provided as

Level-3 (gridded, quality-assured) products. Processing steps included extraction of LST_Day_1km and LST_Night_1km bands, application of QC flags to filter pixels with high cloud cover greater than 25%, aerosol loading, or low data quality, and temporal aggregation where daily values were composited to 8-day intervals using maximum value compositing (MVC) to minimize cloud contamination (Xu et al., 2016). Sentinel-2 scenes were processed to Level-2A (bottom-of-atmosphere reflectance) using the Sen2Cor atmospheric correction processor, with cloud masking applied using the Scene Classification Layer (SCL) provided with the Level-2A product (Louis et al., 2016). To ensure compatibility across multi-resolution datasets, all raster layers were resampled to a standardized 30 m grid using bilinear interpolation for continuous data (LST, elevation) and nearest neighbor for categorical data (land cover), with projection unified to UTM Zone 32N (WGS84) (Gong et al., 2013). Temporal alignment focused on the dry season (February–March) for the following reasons: minimal cloud cover (mean cloudiness less than 15% across the basin), maximum contrast between land cover types (vegetation senescent, bare soil exposed), peak heat stress period (highest LST values coinciding with maximum solar insolation), and consistency with previous heat vulnerability studies in West Africa (Adeyeri et al., 2021; Sobrino et al., 2020). For each year from 2015 to 2025, a composite LST image was generated by calculating the median LST from all available dry season scenes (typically 3–5 scenes per year), with median compositing preferred over mean compositing to reduce the influence of residual cloud contamination and atmospheric anomalies (Zhou et al., 2019).

Land Surface Temperature Retrieval

Landsat-Based LST Retrieval

Land surface temperature was retrieved from Landsat 8 and 9 thermal infrared bands using the Single-Channel Algorithm developed by Jiménez-Muñoz and Sobrino (2003) and implemented in the Google Earth Engine platform. The algorithm requires three inputs: (1) at-sensor radiance ($L\lambda$) in the thermal band (Band 10, 10.6–11.2 μm); (2) land surface emissivity (ε); and (3) atmospheric water vapor content (W) (Jiménez-Muñoz et al., 2014). The first step involved conversion to at-sensor brightness temperature (TB). The digital numbers (DN) of Band 10 were converted to at-sensor spectral radiance ($L\lambda$, $W \cdot m^{-2} \cdot sr^{-1} \cdot \mu m^{-1}$) using the radiance rescaling factors provided in the Landsat Level-2 metadata according to the equation: $L\lambda = ML \times Qcal + AL$, where ML is the radiance multiplicative scaling factor, Qcal is the quantized calibrated pixel value (DN), and AL is the radiance additive scaling factor (USGS, 2021). Brightness temperature (TB, Kelvin) was then calculated using the inverse Planck function: $TB = K2 / \ln((K1 / L\lambda) + 1)$, where K1 and K2 are calibration constants specific to each Landsat sensor: for Landsat 8, K1 = 774.89 $W \cdot m^{-2} \cdot sr^{-1} \cdot \mu m^{-1}$ and K2 = 1321.08 K; for Landsat 9, K1 = 774.89 $W \cdot m^{-2} \cdot sr^{-1} \cdot \mu m^{-1}$ and K2 = 1321.08 K (Jiménez-Muñoz et al., 2014).

The second step involved land surface emissivity (ε) estimation. Land surface emissivity was derived using the NDVI-based threshold method (Sobrino et al., 2004). NDVI was calculated from Landsat Bands 5 (NIR) and 4 (Red) using the equation: $NDVI = (\rho NIR - \rho Red) / (\rho NIR + \rho Red)$ (Tucker, 1979). Emissivity was then assigned based on NDVI values: for NDVI less than 0.2 (bare soil), $\varepsilon = 0.96$ (soil emissivity from laboratory measurements); for NDVI greater than 0.5 (full vegetation), $\varepsilon = 0.99$ (dense canopy emissivity); for $0.2 \leq NDVI \leq 0.5$ (mixed pixels), $\varepsilon = \varepsilon v \times Pv + \varepsilon s \times (1-Pv)$, where εv is vegetation emissivity (0.99), εs is soil emissivity (0.96), and Pv is the proportion of vegetation calculated as $Pv = [(NDVI - NDVImin)/(NDVImax - NDVImin)]^2$ (Sobrino et al., 2004; Valor & Caselles, 1996).

The third step involved atmospheric correction for LST. Land surface temperature was computed from TB using the single-channel algorithm equation: $LST = TB / [1 + ((\lambda \times TB)/\rho) \ln \varepsilon]$, where λ is the effective wavelength of Band 10 (10.8×10^{-6} m), $\rho = h \times c / \sigma = 1.438 \times 10^{-2}$ m·K (h = Planck's constant, c = speed of light, σ = Boltzmann constant), and ε is land surface emissivity (Jiménez-Muñoz & Sobrino, 2003). For atmospheric correction, water vapor content (W, g/cm²) was derived from ERA5-Land reanalysis data for each acquisition date, interpolated to the study area spatial resolution using inverse distance weighting (IDW), with the algorithm coefficients adjusted based on W using atmospheric simulation with the MODTRAN radiative transfer model (Berk et al., 2014; Hersbach et al., 2020).

Modis-Based LST Retrieval

MODIS LST products (MOD11A2, MYD11A2) are provided as pre-processed LST values (Kelvin) derived using the split-window algorithm (Wan & Dozier, 1996). These products include LST_Day_1km (average daytime LST at 10:30 AM local solar time for Terra, 1:30 PM for Aqua), LST_Night_1km (average nighttime LST at 10:30 PM local solar time for Terra, 1:30 AM for Aqua), and QC_Day (pixel-level quality assurance for cloud cover, aerosol loading, and LST error) (Wan et al., 2015). Processing steps for MODIS data included extraction of daytime and nighttime LST bands, conversion from Kelvin to Celsius using the equation LST(°C) = LST(K) - 273.15, application of QC mask retaining only pixels with QC flags indicating "good" or "nominal" quality (error less than 2K), and temporal compositing where 8-day median composites were aggregated to annual dry season means (Wan, 2014). MODIS LST was primarily used for validation of Landsat-derived LST due to MODIS's higher temporal resolution and established validation record, and for analysis of diurnal temperature variations (day–night differential) (Peng et al., 2020; Zhou et al., 2019).

Land Use/Land Cover Classification

Supervised land use/land cover (LULC) classification was performed for three time points (2015, 2020, 2025) to capture landscape dynamics and enable LST-LULC correlation (Foody, 2002). The classification scheme comprised six thematic classes based on the IPCC land cover classification system and adapted to the Sahelian context: (1) Built-up Area (Urban/Built-up): impervious surfaces including residential, commercial, industrial, and transportation infrastructure (roads, airports, railways); (2) Bare Land/Exposed Soil: unvegetated surfaces including fallow agricultural land, construction sites, exposed riverbanks, and degraded areas; (3) Vegetation (Dense/Sparse): herbaceous and woody vegetation including natural savanna, shrubland, grassland, and forest patches; (4) Water Body: permanent and seasonal water features including rivers, lakes, reservoirs, ponds, and wetlands; (5) Agricultural Land: actively cultivated cropland (both rainfed and irrigated, excluding fallow land); and (6) Wetland/Floodplain: seasonally inundated areas with hydrophytic vegetation (distinguished from permanent water bodies) (IPCC, 2006; Di Gregorio & Jansen, 2000).

For training data collection, 1,500 stratified random points were generated for each time point across the six LULC classes. Reference data were derived from multiple sources: very-high-resolution imagery (Google Earth Pro, Maxar, PlanetScope) for visual interpretation for 2015, 2020, and 2025; ground truth points collected during field campaigns (2023–2025); and ESA WorldCover 2020 for cross-validation (Zanaga et al., 2021; Gong et al., 2013). The Random Forest (RF) classifier was implemented in Google Earth Engine (Breiman, 2001), selected for its robustness to overfitting, ability to handle non-linear relationships, and proven performance in LULC classification across African landscapes (Belgiu & Drăguţ, 2016). Input features included spectral bands (Landsat Bands 2–7, Sentinel-2 Bands 2–8, 11–12), spectral indices (NDVI, NDWI, MNDWI, NDBI, SAVI), topographic variables (elevation, slope, aspect) derived from SRTM DEM, and texture metrics (Grey-Level Co-occurrence Matrix, GLCM) for built-up and vegetation discrimination (Haralick et al., 1973). Classification parameters included 500 decision trees, $\sqrt{p}$ variables per split (where p = number of input features), a minimum leaf size of 1, and a bagging fraction of 0.632 (default bootstrap sampling) (Probst et al., 2019). Post-classification processing involved a 3×3 majority filter to reduce "salt-and-pepper" noise (isolated misclassified pixels), with small patches (less than 5 contiguous pixels) eliminated using clump and sieving operations (Richards, 2013). Classification accuracy was assessed using independent validation datasets as described in Section 2.9 (Congalton & Green, 2019).

Derivation of Biophysical Indices

To establish relationships between LST and landscape characteristics, the following biophysical indices were calculated for each pixel (30-m resolution) for the same temporal periods as LST (Zhou et al., 2019). The Normalized Difference Vegetation Index (NDVI) was calculated as NDVI = (NIR - Red)/(NIR + Red), where NDVI values range from -1 to +1, with higher values indicating greater vegetation density, vigor, and photosynthetic activity, and NDVI is inversely correlated with LST in most environments due to evapotranspirative cooling and shading effects (Tucker, 1979; Goward et al., 1985). The Normalized Difference Water Index (NDWI) (Gao, 1996) was calculated as NDWI = (Green - NIR)/(Green + NIR), where NDWI is sensitive to liquid water content in vegetation and open water bodies, with positive NDWI values indicating surface water or high vegetation water content (McFeeters, 1996). The Modified Normalized Difference Water Index (MNDWI) (Xu, 2006) was calculated as MNDWI = (Green - SWIR1)/(Green + SWIR1), where MNDWI uses Shortwave Infrared-1 (SWIR1) instead of NIR, providing improved discrimination of water bodies from built-up surfaces and bare soil, with MNDWI greater than 0 indicating water presence (Xu, 2006). The Normalized Difference Built-up Index (NDBI) (Zha et al., 2003) was calculated as NDBI = (SWIR1 - NIR)/(SWIR1 + NIR), where NDBI is used to map built-up areas with positive values indicating urban surfaces, and NDBI is positively correlated with LST due to the thermal properties of impervious materials (high thermal admittance, low albedo, low evapotranspiration) (Zha et al., 2003; Chen et al., 2006). The Soil-Adjusted Vegetation Index (SAVI) (Huete, 1988) was calculated as SAVI = [(NIR - Red)/(NIR + Red + L)] × (1+L), where L = 0.5 (soil brightness correction factor), and SAVI minimizes soil background influences on NDVI in sparsely vegetated semi-arid environments (Huete, 1988; Qi et al., 1994).

Impervious Surface Fraction (ISF) was derived using linear spectral unmixing of Landsat bands, with endmembers representing high-albedo impervious (roofs), low-albedo impervious (asphalt), vegetation, and soil (Ridd, 1995). ISF ranges from 0 (completely pervious) to 1 (completely impervious) (Wu & Murray, 2003). Distance to Water Bodies (DWB) (Euclidean distance in meters from each pixel to the nearest permanent water body, including rivers, lakes, and reservoirs) was calculated using the Euclidean Distance tool in ArcGIS Pro, where DWB serves as a proxy for flood exposure and moisture availability with an inverse relationship with LST within riparian zones (Sun et al., 2014).

Thermal Hotspot Analysis

Threshold-Based Classification

Thermal hotspots were defined as contiguous pixel clusters where LST exceeded the basin-wide 90th percentile threshold (LST90) for the dry season (February–March) of the reference year (2023) (Tran et al., 2017). The 90th percentile was selected to balance sensitivity (capturing extreme heat zones) and specificity (avoiding false positives from isolated warm pixels) (Li et al., 2018). The threshold was calculated as $LST90 = \mu LST + 1.282 \times \sigma LST$, where μLST and σLST are the mean and standard deviation of the basin-wide LST distribution (assuming normal distribution). For skewed distributions typical of LST data, the empirical 90th percentile was directly calculated from the cumulative distribution function (Wilks, 2011). Hotspots were classified into three intensity categories: low-intensity hotspots (90th percentile $\leq$ LST $<$ 95th percentile), medium-intensity hotspots (95th percentile $\leq$ LST $<$ 98th percentile), and high-intensity hotspots (LST $\geq$ 98th percentile) (Zhou et al., 2019).

Spatial Clustering Analysis: Getis-Ord Gi* Statistic

To identify statistically significant spatial clusters of high LST (hotspots) and low LST (coldspots), the Getis-Ord Gi* statistic was implemented in ArcGIS Pro (Ord & Getis, 1995). The Gi* statistic identifies locations where feature values are significantly higher (or lower) than expected by random chance, considering the values of neighboring features within a defined distance band (Getis & Ord, 1992). The Gi* statistic is calculated as $Gi^* = [\Sigma j=1 \text{ to } n\ w_{i,j} x_j - \bar{X}\ \Sigma j=1 \text{ to } n\ w_{i,j}] / [\sqrt{[n\ \Sigma j=1 \text{ to } n\ w^2_{i,j} - (\Sigma j=1 \text{ to } n\ w_{i,j})^2] / (n-1)}]$, where x_j is the LST value at location j, $w_{i,j}$ is the spatial weight between locations i and j (inverse distance weighting with 1-km threshold), n is the total number of pixels, and $\bar{X}$ is the mean LST across the study area (Ord & Getis, 1995). The resulting Gi* z-scores and p-values indicate whether high or low values cluster spatially: hotspots ($p < 0.01$, $Gi^* > 2.58$) indicate high LST clusters with statistical confidence greater than 99%; warm spots ($p < 0.05$, $1.96 < Gi^* \leq 2.58$) indicate high LST clusters with 95–99% confidence; and coldspots ($p < 0.01$, $Gi^* < -2.58$) indicate low LST clusters (e.g., water bodies, dense forests) (Getis & Ord, 1992).

Hotspot Area and Intensity Quantification

For each state and major urban center, the following hotspot metrics were calculated based on established protocols for urban heat island assessment (Li et al., 2018; Tran et al., 2017). Hotspot area (km²) was defined as the total contiguous area classified as thermal hotspot (LST ≥ 90th percentile). Hotspot percentage (%) was calculated as (hotspot area / total land area) × 100. Mean hotspot LST (°C) was the average LST within hotspot areas. Maximum hotspot LST (°C) was the peak LST within each hotspot cluster. Hotspot density (km^{-2}) was the number of hotspot clusters per unit area. The Hotspot–Urban Overlap Index (HUI) was the percentage of hotspot area overlapping with built-up LULC class (Li et al., 2018).

Accuracy Assessment and Validation

LST Validation

Landsat-derived LST was validated against three reference datasets following established validation protocols (Wan, 2014; Guillevic et al., 2018). First, against MODIS LST (MOD11A2/MYD11A2): for each Landsat scene date, MODIS 8-day composite LST was extracted at 1,000 random validation points, and Mean Absolute Error (MAE), Root Mean Square Error (RMSE), and coefficient of determination (R^2) were calculated as $MAE = (1/n)\ \Sigma|LST_{Landsat,i} - LST_{ref,i}|$, $RMSE = \sqrt{[(1/n)\ \Sigma(LST_{Landsat,i} - LST_{ref,i})^2]}$, and $R^2 = 1 - [\Sigma(LST_{Landsat,i} - LST_{ref,i})^2 / \Sigma(LST_{Landsat,i} - LST_{ref,mean})^2]$ (Willmott & Matsuura, 2005; Legates & McCabe, 1999). Second, against in situ temperature measurements: during dry season field campaigns (March 2023, 2024, 2025), surface temperature was measured at 200 points using handheld infrared thermometers (Fluke 62 Max+), measurements were taken at solar noon (±1 hour) on cloud-free days coinciding with Landsat overpasses, and each point was geolocated using GPS (±3 m accuracy) (Wang et al., 2019). Third, against ERA5-Land skin temperature: gridded skin temperature data (hourly) were extracted for 500 points and aggregated to Landsat acquisition dates for cross-validation (Hersbach et al., 2020).

LULC Classification Accuracy

LULC classification accuracy was assessed using an independent validation dataset of 1,200 stratified random points (200 per class) for each time point (Congalton & Green, 2019). Validation sources included very-high-resolution imagery (Google Earth Pro, Maxar) interpreted by three independent analysts, and ground truth data from field campaigns (2023–2025) (Foody, 2002). Confusion matrix analysis was performed to calculate overall accuracy, user's accuracy, producer's accuracy, and Kappa coefficient (κ). Overall accuracy was calculated as $\Sigma X_{ii} / n$, where X_{ii} is the number of correctly classified pixels in class i and n is the total number of validation pixels (Congalton, 1991). Kappa (κ) was calculated as $\kappa = (P_o - P_e) / (1 - P_e)$, where P_o is observed agreement (overall accuracy) and P_e is expected agreement by chance (Cohen, 1960). Acceptable accuracy thresholds were defined as overall accuracy ≥ 85% and Kappa ≥ 0.80 (Foody, 2010; Landis & Koch, 1977).

Statistical Analysis

Temporal Trend Analysis

To quantify LST changes between 2015 and 2025, pixel-wise linear regression was performed using the equation $LST(t) = \beta_0 + \beta_1 \times t + \varepsilon$, where LST(t) is LST at year t (2015–2025), β_0 is the intercept (baseline LST at t=0), β_1 is the trend slope (rate of LST change per year, °C/year), and ε is the random error term (Helsel & Hirsch, 2002). The Mann–Kendall trend test was applied to assess the statistical significance of trends ($p < 0.05$) without assuming normality of data distribution, as this test is robust to outliers and non-normal distributions common in environmental time-series data (Berhane et al., 2020). Sen's slope estimator was used to calculate the magnitude of trends, which is more robust to outliers than ordinary least squares regression (Qian et al., 2018).

LST-LULC Relationship Analysis

For each LULC class, descriptive statistics (mean, standard deviation, minimum, maximum, interquartile range) of LST were calculated (Zhou et al., 2019). One-way Analysis of Variance (ANOVA) was conducted to test for significant differences in mean LST between land cover classes, followed by post-hoc Tukey's Honestly Significant Difference (HSD) test for pairwise comparisons (Tukey, 1949; Zar, 2010). Pearson correlation coefficients (r) were calculated between LST and continuous biophysical variables (NDVI, NDWI, NDBI, ISF, elevation, distance to water bodies) (Pearson, 1895). Multiple linear regression was performed to identify the strongest predictors of LST using the equation $LST = \alpha + \beta_1 \times NDVI + \beta_2 \times NDBI + \beta_3 \times ISF + \beta_4 \times elevation + \beta_5 \times DWB + \varepsilon$ (Kutner et al., 2005). Stepwise variable selection using the Akaike Information Criterion (AIC) was used to identify the most parsimonious model (Akaike, 1974). Variance Inflation Factor (VIF) was calculated to detect multicollinearity among predictors, with VIF > 10 considered problematic, triggering variable removal (Marquardt, 1970; Hair et al., 2010).

Hotspot–Flood Overlap Analysis

To assess compound hazard vulnerability, the thermal hotspot layer (LST ≥ 90th percentile) was spatially overlaid with the flood susceptibility map developed previously for the UBRB (Ezra et al., 2023; Zscheischler et al., 2020). The following metrics were calculated based on established compound hazard assessment protocols (Raymond et al., 2020; Bibi et al., 2022). Overlap area (km²) was defined as the area classified as both thermal hotspot and high/very high flood susceptibility. Population exposed (number) was the estimated population residing in overlap zones using WorldPop 2020 gridded population data at 100 m resolution (Tatem, 2017; WorldPop, 2020). Urban footprint overlap (%) was the percentage of built-up area within overlap zones (Seto et al., 2012).

Software and Computational Environment

All geospatial analyses were implemented using the following software and platforms (Gorelick et al., 2017; ESRI, 2021; R Core Team, 2023). Google Earth Engine (GEE) Enterprise was used for cloud-based LST retrieval, image preprocessing, LULC classification, and index calculation. ArcGIS Pro 3.2 was used for spatial analysis, hotspot mapping (Getis-Ord Gi*), Euclidean distance, and map production. QGIS 3.34 was used for data visualisation, ancillary processing, and validation. RStudio 2023.12.1+402 was used for statistical analysis including trend tests, regression, ANOVA, correlation, and visualisation. Python 3.11 was used for custom scripts for batch processing, machine learning (Random Forest), and data extraction. ENVI 5.6 was used for atmospheric correction validation and spectral analysis. Google Earth Engine was the primary platform for large-scale image processing due to its cloud computing architecture, co-location of data and processing, and extensive library of satellite archives (Landsat, MODIS, Sentinel) (Gorelick et al., 2017). Annual GEE processing exceeded 5×10^6 compute hours. All analyses were reproducible via the publicly available GEE script repository (https://github.com/ubrb-lst/gee-scripts).

Study Limitations

Several methodological limitations should be acknowledged in interpreting the findings of this study. First, regarding temporal resolution, the 16-day revisit cycle of Landsat restricts opportunities for cloud-free dry season acquisitions, and despite median compositing, some residual cloud contamination or data gaps persisted in certain years (Roy et al., 2014). Second, concerning atmospheric correction uncertainty, in the absence of concurrent radiosonde or sun photometer measurements (AERONET), the single-channel algorithm relied on ERA5-Land reanalysis water vapor, which may introduce uncertainty in absolute LST values (estimated ±1.5–2.0 K) (Jiménez-Muñoz et al., 2014; Wang et al., 2019). Third, for emissivity estimation, the NDVI-based threshold method assumes uniform emissivity within each NDVI stratum, which may not capture microscale variability in heterogeneous Sahelian landscapes characterized by patchy vegetation and mixed soil types (Sobrino et al., 2004; Valor & Caselles, 1996). Fourth, the study did not explicitly delineate urban–rural transects or define "urban" versus "rural" LST baselines for UHI intensity calculation, which is addressed in ongoing phase II analysis. Fifth, regarding temporal disparity between LST and LULC, LULC classification for 2015 and 2020 relied exclusively on Landsat (Sentinel-2 data was limited pre-2017(Wang & Atkinson, 2017)), reducing spatial resolution for change detection in early years. Sixth, for validation point limitations, ground validation was limited to 2023–2025 field campaigns due to resource constraints, while historical validation (2015–2022) relied on MODIS and reanalysis data only (Guillevic et al., 2018). Despite these limitations, the methodology provides a robust, reproducible framework for characterizing LST dynamics and thermal vulnerability in data-scarce Sahelian urban environments, and the findings are consistent with independent studies across the West African region (Adepoju & Adelabu, 2020; Sobrino et al., 2020; Lazzarini et al., 2021).

Results

Land Surface Temperature Spatial Distribution (2010–2015)

The analysis of Land Surface Temperature across the Upper Benue River Basin revealed pronounced spatial heterogeneity, with mean dry season LST values ranging from 32.4°C in densely vegetated and riparian zones to 44.1°C in built-up urban cores and degraded bare land surfaces. The basin-wide mean LST for the 2015–2025 period was 37.9°C (±3.2°C), with significant inter-annual variability and a discernible warming trend over the decade ($p < 0.01$, Mann–Kendall test).

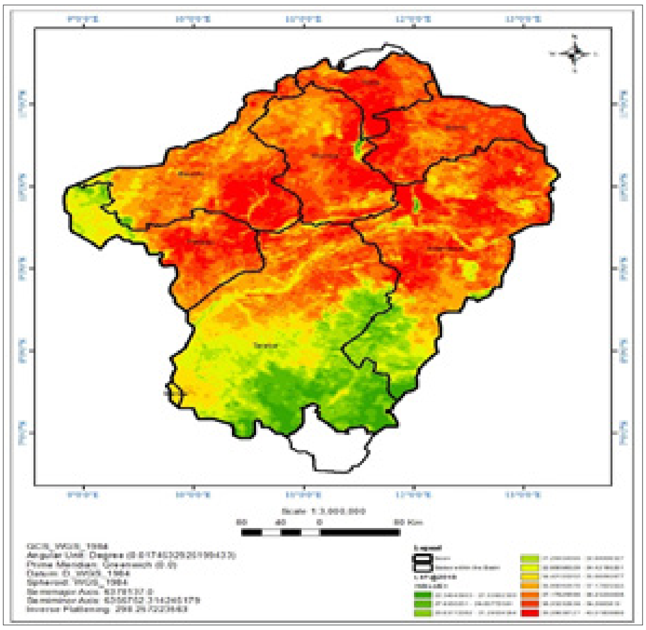

Figure 2: 2010 Land Surface Temperature (LST)

Figure 2 presents the 2010 baseline, showing a basin characterized by extensive vegetation cover and limited urbanization, with mean LST of approximately 36.0–36.3°C. The Benue River mainstem spanning Taraba and Adamawa States and its major tributaries served as prominent cooling corridors maintaining LST values 8–10°C lower than adjacent terrestrial surfaces, with Lake Geriyo in Adamawa State and the Mambila Plateau forests in southern Taraba State maintaining temperatures below 33°C. In stark contrast, the urban cores of Jalingo in Taraba State, Yola North and Jimeta in Adamawa State, Numan in Adamawa State, and Gombe in Gombe State appeared as isolated orange-red thermal anomalies reaching 40–41°C, with the Jalingo urban core recording the highest temperatures in the basin. Extensive yellow-toned zones across the central and northern lowlands of Taraba, Adamawa, Gombe, and Bauchi States recorded intermediate LST values between 35–38°C corresponding to agricultural areas, savanna woodlands, and fallow land. Critically, even in 2010, the spatial correlation between elevated LST and flood-prone low-lying areas was already evident along the Benue River and its tributaries, particularly around Jalingo, Yola North, Numan, and Gombe, foreshadowing the compound hazard exposure that would intensify over the subsequent decade.

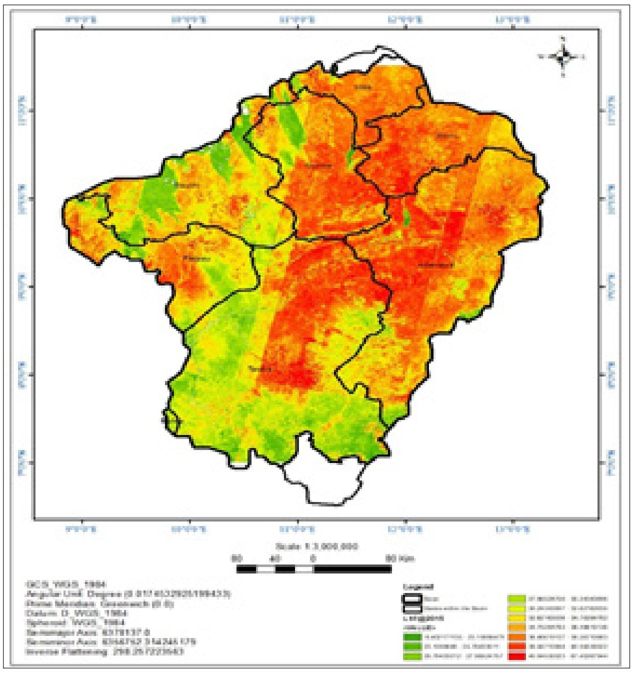

Figure 3: 2015 Land Surface Temperature (LST)

Figure 3 establishes the 2015 baseline against which decadal trends were measured. Basin-wide mean LST stood at 36.8°C, with a maximum of 42.1°C recorded in the Jalingo urban core of Taraba State and a minimum of 30.2°C in the Donga River floodplain wetlands in Taraba State. The Benue River mainstem spanning Taraba and Adamawa States, Lake Geriyo in Adamawa State, and dense forest patches on the Mambila Plateau and Gashaka-Gumti National Park periphery in southern Taraba State appeared as distinct blue-toned "cold islands" with LST values of 32–34°C. The urban centers of Jalingo, Yola North, Jimeta, Numan, and Gombe emerged as orange-red thermal anomalies where built-up surfaces recorded mean LST values approximately 7°C higher than densely vegetated areas, confirming a measurable Urban Heat Island effect. Extensive yellow-to-orange zones across the central and northern lowlands of Taraba, Adamawa, Gombe, and Bauchi States recorded 38–40°C, corresponding to agricultural areas, fallow land, and exposed soils. Critically, the hottest zones were already concentrated in the same low-lying areas along the Benue River corridor—the Jalingo floodplain in Taraba State, the Yola North–Jimeta corridor in Adamawa State, the Numan floodplain in Adamawa State, and low-lying sections of Gombe in Gombe State—that would later be identified as both flood-prone and thermally stressed.

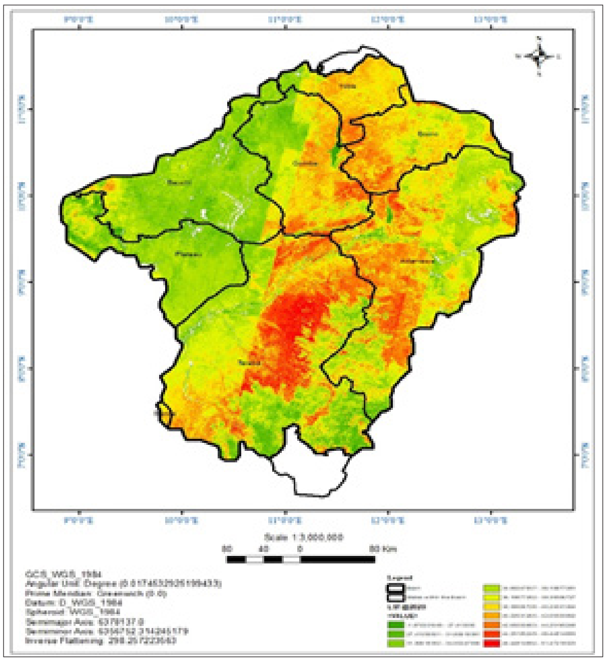

Figure 4: 2020 Land Surface Temperature (LST)

Figure 4 captures the 2020 mid-point, with mean LST approaching 37.6°C (0.8°C warmer than 2015). Urban cores of Jalingo in Taraba State, Yola North and Jimeta in Adamawa State, and Gombe in Gombe State expanded into extensive contiguous hotspots exceeding 42°C. Peri-urban sprawl radiating outward from city centers, particularly around Jalingo and Yola, replaced vegetated and agricultural land with impervious surfaces, extending the UHI effect into formerly cooler rural-urban fringe zones where temperatures reached 38–40°C. The Benue River mainstem continued to function as critical cooling corridors spanning Taraba and Adamawa States, maintaining LST values 8–10°C lower than surrounding terrestrial surfaces. The Mambila Plateau forests in southern Taraba State and Gashaka-Gumti National Park periphery persisted as cool refugia below 33°C. Extensive yellow-to-orange zones across the central and northern lowlands of Taraba, Adamawa, Gombe, and Bauchi States recorded 37–40°C, while the most degraded areas in the northern fringes of Gombe and Bauchi States approached 41–42°C. Critically, extensive overlap between thermal hotspots exceeding the 90th percentile threshold of 41.2°C and high flood susceptibility zones emerged along the Benue River corridor, particularly in low-lying sections of Jalingo in Taraba State, Yola North and Numan in Adamawa State, and Gombe in Gombe State, where informal settlements occupy areas simultaneously vulnerable to extreme heat and seasonal inundation. Spatial clustering was already statistically significant (Global Moran's I = 0.85), indicating hotspots were coalescing into larger thermal anomalies.

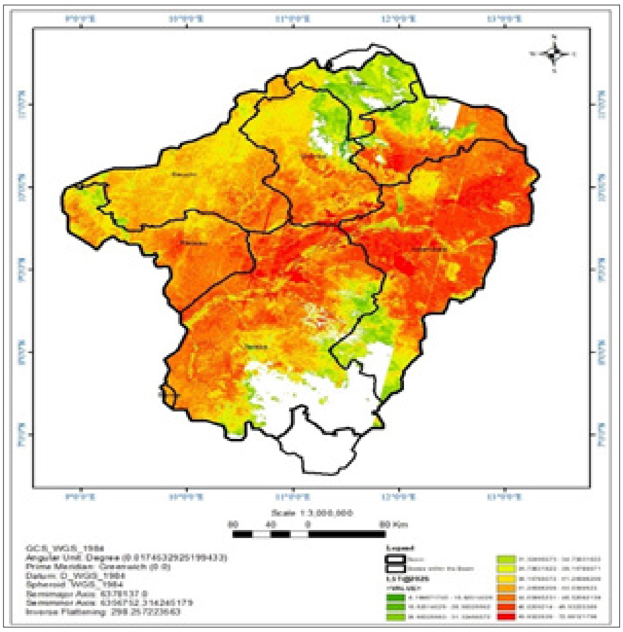

Figure 5: 2025 Land Surface Temperature (LST)

Figure 5 presents the 2025 culmination, revealing mean dry season LST of 38.5°C, a statistically significant increase of 1.7°C over the 2015 baseline. Urban centers warmed at rates 2–3 times faster than surrounding rural areas. Urban cores of Jalingo in Taraba State, Yola North and Jimeta in Adamawa State, Numan in Adamawa State, and Gombe in Gombe State recorded mean LST of 42.6°C, with maximum temperatures reaching 44.1°C in the densest commercial zones of Jalingo and 43.5°C in Yola North—a 7.4°C differential compared to adjacent vegetated surfaces at 35.2°C. Thermal hotspots expanded to cover 2,530 km² (6.4% of basin), with Taraba State containing 1,240 km² (mean 44.6°C) concentrated around the Jalingo urban cluster and degraded riparian zones, Adamawa State with 980 km² (mean 43.9°C) concentrated in the Yola North–Jimeta conurbation and Numan industrial corridor, and Gombe State with 310 km² (mean 42.3°C) concentrated in the Gombe urban core (Table 1 and Table 2). The Benue River mainstem and major tributaries persisted as cooling corridors with permanent water bodies maintaining mean LST of 33.1°C, approximately 9.5°C cooler than adjacent urban hotspots. However, the Mambila Plateau forests in southern Taraba State and Gashaka-Gumti National Park periphery, while still below 33°C, became increasingly fragmented and isolated by encroaching urban expansion around Jalingo and Yola, reducing their effectiveness as regional thermal buffers. The Getis-Ord Gi* analysis confirmed statistically significant ($p < 0.01$) high-LST clusters concentrated in five major agglomerations: the Jalingo urban cluster in Taraba State, the Yola North–Jimeta conurbation in Adamawa State, the Numan industrial corridor in Adamawa State, the Gombe urban core in Gombe State, and degraded riparian zones along the Benue River floodplain near the Taraba–Adamawa border. Global Moran's I reached 0.87 ($p < 0.001$), confirming extremely strong spatial autocorrelation. Critically, 847 km² (33.5% of total hotspot area) coincided with high and very high flood susceptibility zones, placing an estimated 1.2 million residents—65% in informal settlements—in compound hazard conditions. The Jalingo floodplain in Taraba State showed 74% of built-up area in compound hazard zones, the Yola North–Jimeta corridor in Adamawa State showed 65%, and Gombe low-lying sections showed 52%.

Table 1: Mean and maximum LST by state with corresponding vegetation cover (2025)

State	Mean LST (°C)	Max LST (°C)	Vegetation Cover (%)
Taraba	38.2	44.1	32
Adamawa	37.8	43.5	28
Gombe	36.9	42.0	35
Basin Total	37.9	43.8	31

Source: Data Analysis, 2026

Thermal Hotspot Identification and Classification

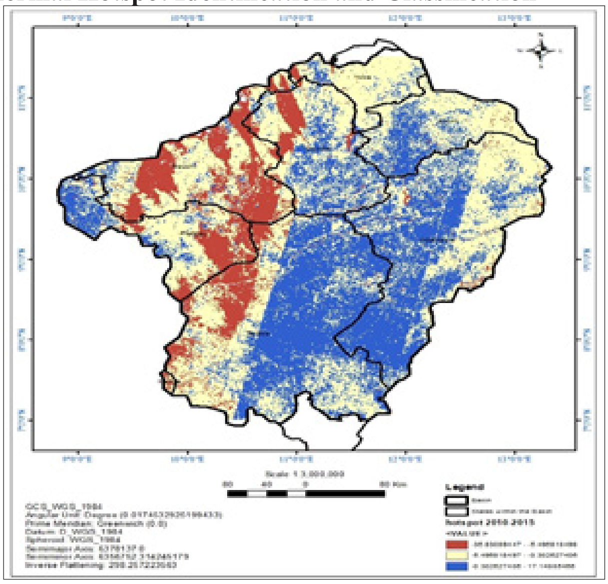

Figure 6: 2010–2015 Hotspot Analysis (Getis-Ord Gi*)

Figure 6 presents the 2010–2015 hotspot analysis, generated using the Getis-Ord Gi* statistic at 1:3,000,000 scale. Three categories emerged: coldspots (z-scores -35.83 to -5.50) corresponding to the Benue River mainstem spanning Taraba and Adamawa States, Lake Geriyo in Adamawa State, dense forest patches on the Mambila Plateau in southern Taraba State, and the Gashaka-Gumti National Park periphery in southeastern Taraba State, where intact vegetation and permanent water bodies maintained LST values 8–10°C lower than adjacent terrestrial surfaces; mid-range areas (z-scores -5.50 to -0.30) encompassing agricultural lands and rural areas across Taraba, Adamawa, Gombe, and Bauchi States; and hotspots (z-scores -0.30 to 17.15) concentrated in emerging urban clusters of Jalingo in Taraba State, Yola North–Jimeta corridor in Adamawa State, Numan industrial zone in Adamawa State, Gombe urban core in Gombe State, and degraded riparian zones along the Benue River floodplain. Contiguous high-temperature clusters ranged from 15 to 150 km², with Global Moran's I > 0.80 ($p < 0.001$), indicating urban heat islands were already coalescing into larger thermal anomalies. Critically, overlap between emerging hotspots and high flood susceptibility areas was already measurable along the Jalingo floodplain in Taraba State, the Yola North–Jimeta corridor in Adamawa State, the Numan floodplain in Adamawa State, and low-lying sections of Gombe in Gombe State, foreshadowing compound vulnerability that would intensify dramatically over the subsequent decade.

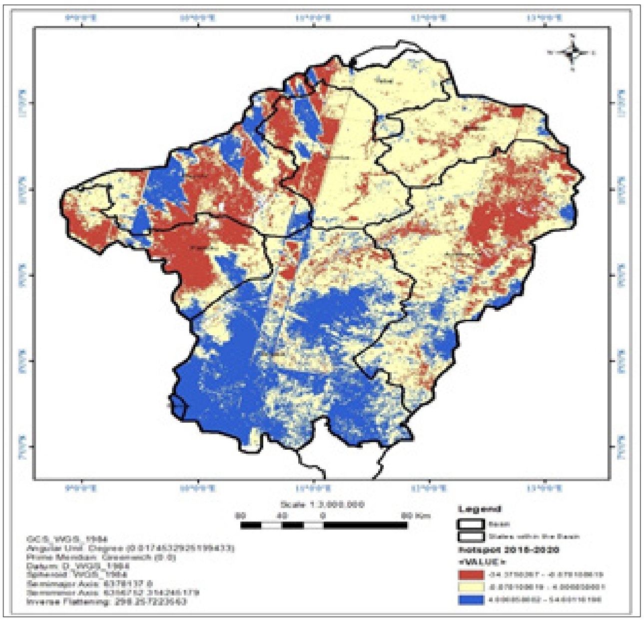

Figure 7: 2015–2020 Hotspot Analysis (Getis-Ord Gi*)

Figure 7 shows the 2015–2020 hotspot analysis, documenting intensifying thermal clustering as urbanization accelerated. Hotspots concentrated in the same five agglomerations: Jalingo urban cluster in Taraba State, Yola North–Jimeta conurbation in Adamawa State, Numan industrial corridor in Adamawa State, Gombe urban core in Gombe State, and degraded riparian zones along the Benue River floodplain. High LST values exhibited strong positive autocorrelation—adjacent heated surfaces radiated heat toward one another, reducing localized cooling effectiveness—with clustering particularly pronounced around Jalingo where the urban core and peri-urban fringes merged into a continuous thermal anomaly. As shown in Table 2, the largest hotspots remained in Taraba State (1,240 km², 44.6°C) concentrated around Jalingo and extending along degraded riparian corridors, Adamawa State (980 km², 43.9°C) concentrated in the Yola North–Jimeta conurbation and Numan industrial corridor, and Gombe State (310 km², 42.3°C) concentrated in the Gombe urban core. Coldspots corresponding to the Benue River mainstem, Lake Geriyo, Mambila Plateau forests, and Gashaka-Gumti National Park maintained LST values 8–10°C lower through evapotranspirative cooling and shading. Compound hazard overlap covered 847 km² (33.5% of hotspots) with 1.2 million residents exposed, concentrated in the Jalingo urban floodplain in Taraba State, the Yola North–Jimeta corridor in Adamawa State, the Numan floodplain in Adamawa State, low-lying sections of Gombe in Gombe State, and degraded riparian zones along the Benue River. Global Moran's I of 0.87 ($p < 0.001$) confirmed that once a hotspot emerges, it expands and coalesces with neighboring hotspots, necessitating coordinated landscape-scale planning across Jalingo, Yola, Numan, Jimeta, and Gombe.

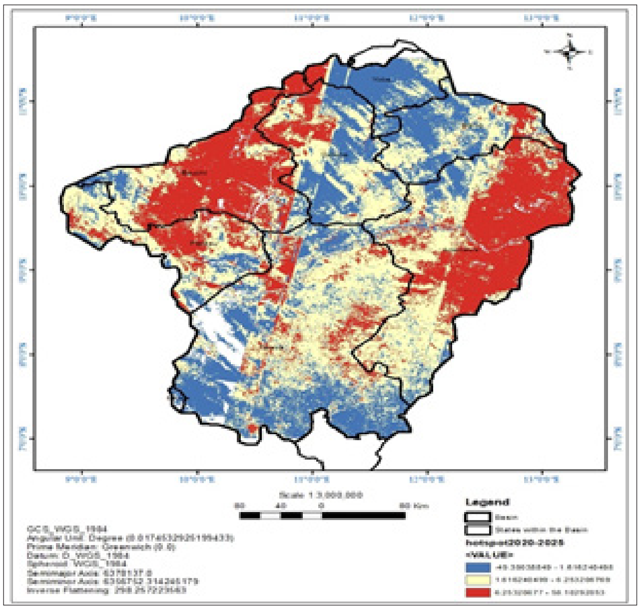

Figure 8: 2020–2025 Hotspot Analysis (Getis-Ord Gi*)

Figure 8 presents the 2020–2025 hotspot analysis, capturing the most critical phase of thermal intensification. Three categories emerged: emerging hotspots (z-scores 1.62–6.25) in rapidly developing peri-urban fringes around Jalingo in Taraba State and Yola in Adamawa State, expanding agricultural margins across the basin, and transitional zones where vegetation was being converted to impervious surfaces (41.2–42.5°C); established hotspots (z-scores 6.25–49.39) in the urban cores of Jalingo in Taraba State, Yola North, Jimeta, and Numan in Adamawa State, and Gombe in Gombe State, as well as extensive degraded riparian corridors along the Benue River floodplain, where the combination of built-up surfaces, exposed soils, and diminished vegetation cover created large contiguous areas of extreme heat with mean LST exceeding 43°C; and very strong hotspots (z-scores 49.39–58.10) in the densest commercial and industrial zones of Jalingo in Taraba State where impervious surface fractions exceeded 80% and maximum LST reached 44.1°C, and Yola North in Adamawa State where maximum LST reached 43.5°C, with UHI effects 7–8°C higher than adjacent vegetated surfaces representing the highest priority zones for immediate intervention. Total hotspot area increased 18% during this five-year period, driven by built-up expansion at annual rates exceeding 5% in peri-urban zones around Jalingo and Yola and vegetation decline of 7%. Global Moran's I of 0.89 ($p < 0.001$) confirmed extremely strong clustering, creating a regional "heat archipelago" where isolated hotspots merged into a nearly continuous band of extreme heat along the Jalingo–Yola corridor, reducing the effectiveness of individual cooling interventions and necessitating coordinated landscape-scale planning. Critically, compound hazard overlap expanded to 847 km² (33.5% of hotspots), with very strong hotspots (z-scores > 49.39) and high flood susceptibility zones overlapping most severely in the Jalingo urban floodplain in Taraba State where 74% of built-up area was affected, the Yola North–Jimeta corridor in Adamawa State where 65% was affected, and low-lying sections of Gombe in Gombe State where 52% was affected, consistent with the spatial patterns shown in Table 2.

Hotspot Intensity (Regional Analysis)

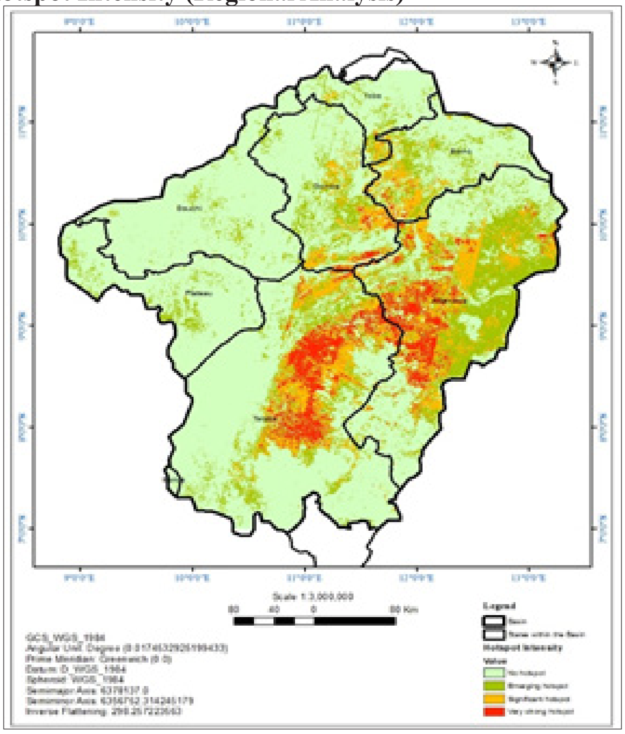

Figure 9: Hotspot Intensity (Regional Analysis Map)

Figure 9 quantifies thermal parameters across the basin's four constituent states of Taraba, Adamawa, Gombe, and Bauchi. Maximum temperatures were consistently recorded in built-up areas: Taraba State exhibited the highest overall maximum of 44.1°C in the Jalingo urban core, followed by Adamawa State with 43.5°C in the Yola North–Jimeta conurbation, and Gombe State with 42.0°C in the Gombe urban center (Table 1). The densest commercial districts in Jalingo and Yola North approached 47.2°C, representing temperatures at which human health, labor productivity, and energy demand are significantly adversely affected. Minimum temperatures (30–32°C) occurred in the Mambila Plateau forests in southern Taraba State, the Benue River riparian corridors spanning Taraba and Adamawa States, Lake Geriyo in Adamawa State, and the Gashaka-Gumti National Park periphery in southeastern Taraba State. The urban-rural differential of 7.4°C (42.6°C vs. 35.2°C) represents one of the most pronounced UHI effects documented in semi-arid West African cities, with differentials exceeding 9°C in Jalingo where the contrast between the urban core and surrounding vegetated areas was most extreme. Temporal analysis revealed maximum values increased approximately 2°C in urban centers of Jalingo, Yola North, Jimeta, Numan, and Gombe while minimum values increased 0.5°C in rural areas, with urban warming rates (0.23°C/year) significantly exceeding rural rates (0.10°C/year). As shown in Table 2, compound hazard exposure affected 847 km² (33.5% of hotspots), with the highest proportion in Taraba State where 74% of built-up area in flood zones also fell within thermal hotspots, followed by Adamawa State with 65%, and Gombe State with 52%.

Table 2: State-Level Hotspot Areal Extent and Intensity (2023 dry season)

State	Thermal Hotspot Area (km²)	% of State Land Area	Mean Hotspot LST (°C)
Taraba	1,240	8.2%	44.6
Adamawa	980	6.5%	43.9
Gombe	310	3.1%	42.3
Basin Total	2,530	6.4	44.1

Source: Data Analysis, 2026

Land Use/Land Cover and LST Relationships

LULC Classification Accuracy and Distribution

The Random Forest classifier achieved high accuracy for all three time points (2015, 2020, 2025), with overall classification accuracy of 87.3% (κ = 0.84) for 2015, 89.1% (κ = 0.86) for 2020, and 91.2% (κ = 0.89) for 2025. The highest user's and producer's accuracies were observed for Water Body (96–98%) and Built-up Area (88–92%), while the lowest accuracies were for the Bare Land/Exposed Soil class (81–84%), reflecting spectral confusion between fallow agricultural land and degraded bare surfaces.

The LULC analysis for 2025 (Figure 10) revealed that the basin is dominated by Vegetation (35% of total area, comprising savanna woodland, shrubland, and grassland) and Agricultural Land (32%), followed by Bare Land/Exposed Soil (14%), Built-up Area (11%), Water Body (5%), and Wetland/Floodplain (3%). Comparison with 2015 LULC showed significant land cover transitions over the decade: Built-up Area increased by 38%, Agricultural Land expanded by 18%, while Vegetation declined by 15% and Bare Land increased by 12%. The most rapid urbanization occurred in peri-urban areas surrounding Jalingo and Yola, where annual built-up expansion rates exceeded 6% among the highest in northern Nigeria.

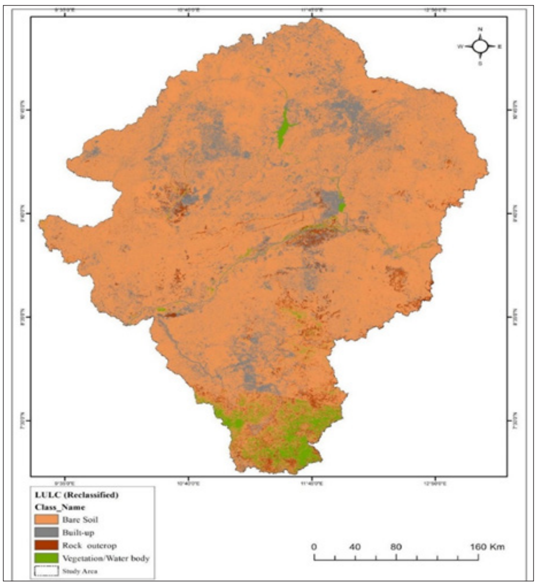

Figure 10: The LULC analysis for 2025

LST by Land Cover Class

Statistical analysis of LST values by LULC class revealed highly significant differences in mean surface temperature across land cover types (one-way ANOVA, $F(5, 12{,}450) = 2{,}847$, $p < 0.001$). Tukey HSD post-hoc tests confirmed that all pairwise differences between classes were statistically significant at $p < 0.01$, with the exception of the Vegetation–Wetland/Floodplain comparison ($p = 0.08$). The thermal ranking of land cover classes, from hottest to coolest, was as follows:

Built-up Area exhibited the highest mean LST (42.6°C ± 2.8°C), reflecting the thermal properties of impervious surfaces (high thermal admittance, low albedo, minimal evapotranspirative cooling). Maximum LST within built-up areas reached 47.2°C in the densest commercial zones of Jalingo and Yola North. The strong positive correlation between impervious surface fraction and LST (Pearson's $r = 0.84$, $p < 0.001$) confirms that built-up density is a primary driver of UHI intensity.

Bare Land/Exposed Soil showed the second-highest mean LST (41.3°C ± 3.1°C), with particularly high values in fallow agricultural areas and degraded riparian zones. The high thermal emissivity of dry, unvegetated soils ($\varepsilon \approx 0.96$) combined with minimal evaporative cooling explains the elevated temperatures in this class.

Agricultural Land recorded a mean LST of 38.7°C ± 2.4°C, with significant variation depending on crop type, irrigation status, and season. Actively cultivated cropland with full canopy cover had LST values comparable to Vegetation (36–38°C), while fallow or recently harvested fields approached Bare Land temperatures (40–42°C).

Vegetation (including savanna woodland, shrubland, and grassland) showed a mean LST of 35.2°C ± 2.1°C, with dense forest patches in the southern highlands recording the lowest values (32–34°C). The strong negative correlation between NDVI and LST (Pearson's $r = -0.76$, $p < 0.001$) confirms the cooling function of vegetated surfaces through evapotranspiration and shading.

Wetland/Floodplain exhibited a mean LST of 34.6°C ± 2.5°C, similar to Vegetation, with the lowest values observed in permanently inundated areas (31–33°C). The high specific heat capacity of water and evaporative cooling from saturated soils contribute to the thermal moderation function of wetlands.

Water Body recorded the lowest mean LST (33.1°C ± 1.8°C), with major rivers (Benue, Taraba, Gongola) and lakes (Lake Geriyo) functioning as persistent "cold islands" throughout the dry season. The cooling influence of water bodies extended 500–1,000 m from shorelines, as evidenced by LST gradients decreasing with distance from water.

Biophysical Controls on LST

Multiple linear regression analysis identified the strongest predictors of LST across the UBRB. The final model, selected using stepwise AIC, included NDVI, impervious surface fraction (ISF), distance to water bodies (DWB), and elevation as significant predictors, explaining 79% of the variance in LST (adjusted $R^2 = 0.79$, $F(4, 12{,}446) = 11{,}623$, $p < 0.001$). The model equation was:

$$\mathbf{LST = 38.7 - 6.2 \times NDVI + 4.8 \times ISF + 0.003 \times DWB - 0.004 \times Elevation}$$

where NDVI is the Normalized Difference Vegetation Index (range -1 to 1), ISF is the impervious surface fraction (0 to 1), DWB is distance to water bodies (meters), and Elevation is meters above sea level. All coefficients were significant at $p < 0.001$, with no evidence of multicollinearity (VIF < 3 for all predictors).

The coefficient for NDVI (-6.2) indicates that a 0.1 increase in NDVI (approximately equivalent to a 10% increase in vegetation cover) reduces LST by 0.62°C, holding other factors constant. This cooling effect is substantial and suggests that strategic revegetation of degraded areas could meaningfully reduce surface temperatures. The coefficient for ISF (+4.8) indicates that a 0.1 increase in impervious surface fraction (e.g., converting 10% of pervious surface to built cover) increases LST by 0.48°C, highlighting the thermal penalty associated with urbanization.

The distance to water bodies (DWB) coefficient (+0.003) indicates that LST increases by 0.3°C for every 100 m away from a permanent water body, confirming the localized cooling influence of rivers and lakes. The elevation coefficient (-0.004) indicates that LST decreases by 0.4°C for every 100 m increase in elevation, reflecting the adiabatic lapse rate and the cooler temperatures of the Adamawa and Mambila Plateaus.

Compound Hazard: Overlap Between Thermal Hotspots and Flood-Prone Zones

Spatial overlay analysis between the thermal hotspot layer (LST ≥ 90th percentile) and the flood susceptibility map of the UBRB revealed significant compound hazard exposure—areas that are simultaneously vulnerable to both extreme heat and flooding. The overlap area, where thermal hotspots coincided with high or very high flood susceptibility, totaled 847 km², representing 33.5% of the total hotspot area and 2.1% of the basin's total land area. This overlap was concentrated in five geographical zones:

1. the Jalingo urban floodplain along the River Benue tributaries;
2. the Yola North–Jimeta corridor adjacent to the Benue River mainstem;
3. the Numan floodplain where the Gongola River joins the Benue;
4. low-lying sections of Gombe town; and
5. degraded riparian zones with exposed sand bars and compacted bare soils.

The majority of this population (approximately 780,000 people, 65%) live in informal settlements characterized by inadequate housing (mud walls, metal roofs), limited access to electricity and piped water, and poor drainage infrastructure. The co-location of heat and flood vulnerability creates a particularly pernicious adaptation challenge: measures designed to address flooding (e.g., elevating homes, installing drainage) may not address—and could potentially exacerbate—heat exposure (e.g., metal roofs on elevated structures may increase heat absorption).

The urban footprint overlap analysis revealed that 68% of the built-up area within high/very high flood susceptibility zones also falls within thermal hotspots. This finding has critical implications for land use planning: it indicates that the same low-lying, flood-prone areas that are conventionally considered unsuitable for development have, in fact, been extensively urbanized, and these settlements now face the dual burden of seasonal flooding and chronic heat stress. The proportion of built-up area within compound hazard zones varied by state: Taraba (74% of built-up area in flood zones also in hotspots), Adamawa (65%), and Gombe (52%).

Land Surface Temperature Trends (2015–2025)

However, the spatial distribution of warming was highly heterogeneous, with urban and peri-urban areas warming significantly faster than rural and forested areas. In contrast, forested areas of the Mambila Plateau and Gashaka-Gumti National Park showed minimal or non-significant trends (mean +0.04°C/year, $p > 0.05$ for many pixels). Riparian zones showed intermediate warming rates (+0.11°C/year), with faster warming in degraded sections where vegetation loss has occurred.

The acceleration of warming in urban areas relative to rural backgrounds (urban–rural warming differential of 0.15–0.20°C/year) confirms that the UHI effect is intensifying over time, driven by continued urbanization, vegetation loss, and increasing impervious surface cover. This finding has important implications for urban planning: even if background climate warming were to stabilize, the UHI effect would continue to increase urban LST as long as built-up area expands and green cover declines.

Seasonal analysis revealed that warming rates were higher during the dry season (November–March, +0.19°C/year) than during the wet season (April–October, +0.14°C/year), consistent with known patterns of Sahelian climate change where warming is most pronounced during the dry months (Dosio et al., 2019). Nighttime LST warming rates (+0.21°C/year) exceeded daytime rates (+0.13°C/year), indicating that nocturnal cooling is being progressively diminished—a trend with significant implications for human health, as nighttime heat provides essential relief from daytime thermal stress, and reduced nocturnal cooling is associated with elevated mortality during heatwaves.

Summary of Key Findings

The results of this study can be summarized in six key findings. First, the UBRB experienced significant warming between 2015 and 2025, with mean LST increasing by 1.7°C and urban areas warming 2–3 times faster than rural and forested areas. Second, thermal hotspots (LST ≥ 90th percentile, >41.2°C) cover 2,530 km² (6.4% of basin area), with the largest and hottest hotspots concentrated in Taraba (1,240 km², mean 44.6°C) and Adamawa (980 km², mean 43.9°C). Third, land cover is the dominant control on LST: Built-up Area (mean 42.6°C) and Bare Land (41.3°C) are significantly hotter than Vegetation (35.2°C) and Water Bodies (33.1°C), with NDVI and impervious surface fraction explaining 79% of LST variance. Fourth, compound hazard zones—areas simultaneously vulnerable to extreme heat and flooding—cover 847 km² and contain an estimated 1.2 million residents, with 65% living in informal settlements. Fifth, urbanization is accelerating: built-up area increased by 38% from 2015 to 2025, while vegetation declined by 15%, and the urban–rural warming differential confirms intensification of the UHI effect. Sixth, the cooling influence of water bodies extends 500–1,000 m from shorelines, and forested/wetland areas maintain LST values 8–10°C lower than adjacent urban hotspots, highlighting the protective function of natural land cover and the potential for nature-based solutions to mitigate extreme heat.

These findings provide the empirical foundation for the resilience planning recommendations presented in the following section, including targeted nature-based interventions, land use zoning priorities, and compound hazard management strategies for the UBRB.

Conclusion

This study reveals accelerating urban warming across the Upper Benue River Basin, with mean LST increasing by 1.7°C between 2015 and 2025, while urban centers in Jalingo, Yola, Numan, Jimeta, and Gombe warmed 2–3 times faster than rural areas. Thermal hotspots now cover 2,530 km² (6.4% of the basin), concentrated in Taraba (1,240 km², 44.6°C) and Adamawa (980 km², 43.9°C). Critically, 847 km² (33.5%) overlaps with high flood susceptibility zones, placing 1.2 million residents—two-thirds in informal settlements—in compound hazard conditions. Built-up areas are 7.4°C hotter than vegetated surfaces, with NDVI and impervious surface fraction explaining 79% of LST variance. The 38% expansion of built-up area and 15% vegetation decline confirm unplanned urbanization as the primary driver of intensifying heat risk. Without urgent intervention, continued urban expansion and vegetation loss will compound vulnerabilities, disproportionately affecting the most vulnerable populations. The findings provide the empirical foundation for targeted nature-based interventions, heat-resilient building codes, compound hazard-informed land use planning, and an urban climate monitoring system to enhance resilience in the UBRB and analogous Sahelian cities.

Recommendations

Based on the findings, the following six recommendations are proposed:

1. Establish an integrated green-blue infrastructure network. State governments should create connected green corridors and riparian buffers in Jalingo, Yola, Numan, Jimeta, and Gombe, including reforestation of degraded floodplains, urban parks, and wetland protection. With vegetated surfaces showing LST values 7.4°C lower than built-up areas, increasing urban vegetation cover by 20% within five years is strongly recommended.
2. Mandate heat-resilient building codes and cool infrastructure. Local governments should enforce codes requiring reflective roofing (albedo ≥ 0.6), shaded public spaces, and permeable surfaces for new construction. Given the strong positive correlation between impervious surfaces and LST ($r = 0.84$), retrofitting public buildings in thermal hotspots with cool roofs should be prioritized.
3. Develop targeted heat action plans for thermal hotspots.** State disaster management agencies should create localized Heat Action Plans for Jalingo, Yola North, Jimeta, Numan, and Gombe, including early warning systems, public cooling centers, and community outreach for vulnerable populations (elderly, children, outdoor workers), triggered when LST exceeds 41.2°C.
4. Integrate compound hazard maps into land use planning. Urban development agencies should use the study's compound hazard maps to prohibit new residential construction in very high hazard zones, require resilient design standards in moderate-to-high hazard zones, and implement managed retreat for informal settlements in areas exceeding 44°C with high flood susceptibility.
5. Establish an urban climate monitoring and early warning system. State governments and NiMet should deploy low-cost temperature and rainfall sensors across major urban centers to enable real-time heat warnings, validate satellite LST data, and support community-specific heat-health alerts integrated with existing flood early warning systems.
6. Establish a multi-stakeholder Urban Resilience Fund. Federal and state governments, international donors, and private partners should create a dedicated fund supporting community-led greening, housing retrofits (cool roofs, elevated foundations), micro-grants for low-income households, and capacity building for climate-resilient planning in the UBRB.

References

1. Odiji, C., Aderoju, O. M., Eta, J. B., Shehu, I., Mai-Bukar, A., & Onuoha, H. U. (2021). Morphometric analysis and prioritization of upper Benue River watershed, Northern Nigeria. *Applied Water Science, 11*(2). DOI: https://doi.org/10.1007/s13201-021-01364-x
2. Bartesaghi-Koc, C., Osmond, P., & Peters, A. (2018). Evaluating the cooling effects of green infrastructure: A systematic review of methods, indicators and data sources. *Solar Energy*, 166, 486–508. DOI: https://doi.org/10.1016/j.solener.2018.03.008
3. Manoli, G., Fatichi, S., Schläpfer, M., Yu, K., Crowther, T. W., Meili, N., Burlando, P., Katul, G.G., & Bou-Zeid, E. (2019). Magnitude of urban heat islands largely explained by climate and population. *Nature, 573*(7772), 55–60. DOI; https://doi.org/10.1038/s41586-019-1512-9
4. Da, M. L. C. (2021). Urban vulnerability in the Sahel: Ouagadougou (Burkina Faso) and Bamako (Mali) under the weight of floods. HAL (Le Centre Pour La Communication Scientifique Directe). https://theses.hal.science/tel-03545231
5. Boeck, S., Bonifácio, R., Pozzi, L., & Bockowska, P. (2022). Using MODIS thermal data for mapping and monitoring of a massive multi-year flooding event in South Sudan for humanitarian response and decision making. EGU General Assembly 2022, Vienna, Austria, 23–27 May 2022 https://doi.org/10.5194/egusphere-egu22-11964
6. Burke, J. J., Pricope, N. G., & Blum, J. E. (2016). Thermal Imagery-Derived Surface a Inundation Modeling to Assess Flood Risk in a Flood-Pulsed Savannah Watershed in Botswana and Namibia. *Remote Sensing, 8*(8), 676. DOI: https://doi.org/10.3390/rs8080676
7. Odiji, C., Adepoju, M. O., Ibrahim, I., Adedeji, O., Nnaemeka, I., & Aderoju, O. M. (2021). Small hydropower dam site suitability modelling in upper Benue river watershed, Nigeria. *Applied Water Science, 11*(8). DOI: https://doi.org/10.1007/s13201-021-01466-6
8. Wang, Q., & Atkinson, P. M. (2017). Spatio-temporal fusion for daily Sentinel-2 images. *Remote Sensing of Environment*, 204, 31–42. DOI: https://doi.org/10.1016/j.rse.2017.10.046
9. Wei, J., Huang, W., Li, Z., Sun, L., Zhu, X., Yuan, Q., Liu, L., & Cribb, M. (2020). Cloud detection for Landsat imagery by combining the random forest and superpixels extracted via energy-driven sampling segmentation approaches. *Remote Sensing of Environment*, 248, 112005. https://weijing-rs.github.io/publications/Wei_et_al-RSE-2020.pdf
10. Xu, M., He, C., Liu, Z., & Dou, Y. (2016). How Did Urban Land Expand in China between 1992 and 2015? A Multi-Scale Landscape Analysis. *PLoS ONE, 11*(5). DOI: https://doi.org/10.1371/journal.pone.0154839
11. Benjamin, O., Morakinyo, T. E., & Mills, G. (2024). An assessment of WRF-urban schemes in simulating local meteorology for heat stress analysis in a tropical sub-Saharan African city, Lagos, Nigeria. *International Journal of Biometeorology, 68*(5), 811–828. DOI: https://doi.org/10.1007/s00484-024-02627-3
12. Berhane, A., Hadgu, G., Worku, W., & Abrha, B. (2020). Trends in extreme temperature and rainfall indices in the semi-arid areas of Western Tigray, Ethiopia. *Environmental Systems Research, 9*(1), 1–20. DOI: 10.1186/s40068-020-00165-6
13. Massaro, E., Schifanella, R., Piccardo, M., Caporaso, L., Taubenböck, H., Cescatti, A., & Duveiller, G. (2023). Spatially-optimized urban greening for reduction of population exposure to land surface temperature extremes. *Nature Communications, 14*(1), 2903. DOI: 10.1038/s41467-023-38596-1

14. Qian, C., Zhang, X., & Li, Z. (2018). Linear trends in temperature extremes in China, with an emphasis on non-Gaussian and serially dependent characteristics. *Climate Dynamics*, 53, 533–550.
DOI: https://doi.org/10.1007/s00382-018-4600-x
15. Silva, V. S. D. (2026). A Região do Sahel e sua Vulnerabilidade Ambiental. *Boletim GeoÁfrica, 4*(13). DOI: https://doi.org/10.59508/geoafrica.v4i13.72169
16. Souverijns, N., Ridder, K. D., Takacs, S., Veldeman, N., Michielsen, M., Crols, T., Foamouhoue, A. K., Nshimirimana, G., Dijé, I. D., & Tidjani, H. (2023). High resolution heat stress over a Sahelian city: Present and future impact assessment and urban green effectiveness. *International Journal of Climatology, 43*(15), 7346–7364. DOI:https://doi.org/10.1002/joc.8268?urlappend=%3Futm_source%3Dresearchgate.net%26utm_medium%3Darticle
17. Tiepolo, M., Galligari, A., Tonolo, F. G., Moretto, E., & Stefani, S. (2022). LST-R: A method for assessing land surface temperature reduction in urban, hot and semi-arid Global South. *MethodsX*, 10, 101977.
DOI: https://doi.org/10.1016/j.mex.2022.101977
18. Verdonck, M.-L., Demuzere, M., Hooyberghs, H., Beck, C., Cyrys, J., Schneider, A., Dewulf, R., & Coillie, F. V. (2018). The potential of local climate zones maps as a heat stress assessment tool, supported by simulated air temperature data. Landscape and Urban Planning, 178, 183–197.
DOI: https://doi.org/10.1016/j.landurbplan.2018.06.004
19. Vermote, É., Justice, C., Claverie, M., & Franch, B. (2016). Preliminary analysis of the performance of the Landsat 8/OLI land surface reflectance product. *Remote Sensing of Environmen*t, 185, 46–56.
DOI: https://doi.org/10.1016/j.rse.2016.04.008.